THE JOURNAL OF PHYSICAL CHEMISTRY C

ARTICLE

pubs.acs.org/JPCC

Functionalization of Single-Layer MoS_2 Honeycomb Structures

C. Ataca[†,‡] and S. Ciraci*[,†,‡]

[†]Department of Physics and [‡]UNAM-Institute of Materials Science and Nanotechnology, Bilkent University, Ankara 06800, Turkey

ABSTRACT: Based on first-principles plane-wave calculations, we studied the functionalization of the two-dimensional single-layer MoS_2 structure through adatom adsorption and vacancy defect creation. Minimum-energy adsorption sites were determined for 16 different adatoms, each of which gives rise to diverse properties. Bare, single-layer MoS_2, which is normally a nonmagnetic, direct-band-gap semiconductor, attains a net magnetic moment upon adsorption of specific transition-metal atoms, as well as silicon and germanium atoms. The localized donor and acceptor states in the band gap expand the utilization of MoS_2 in nanoelectronics and spintronics. Specific adatoms, such as C and O, attain significant excess charge upon adsorption onto single-layer MoS_2, which might be useful for tribological applications. Each MoS_2 triple vacancy created in a single layer of MoS_2 gives rise to a net magnetic moment, whereas other vacancy defects related to Mo and S atoms do not influence the nonmagnetic ground state. The present results are also relevant for the surface of graphitic MoS_2.

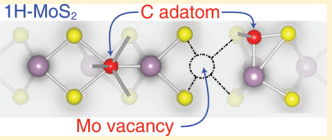

INTRODUCTION

The synthesis of flakes of molybdenum disulfide, MoS_2, has been subject of interest because of the unique symmetry of its honeycomb structure and its esoteric binding mechanism.[1−3] Recently, two-dimensional suspended single-layer MoS_2 sheets (specified as 1H-MoS_2) have been produced.[1,4,5] Single-layer MoS_2 nanocrystals of ∼30-Å width were also synthesized on Au(111) surface.[2] Liquid exfoliation of nanosheets of MoS_2 and other transition-metal dichalcogenides, such as $MoSe_2$, WS_2, $MoTe_2$, $NbSe_2$, and $NiTe_2$, has been reported.[6] 1H-MoS_2 is made up of hexagons with Mo and two S atoms situated at alternating corners. Recently, this material with its nanoribbons has been the subject of several theoretical studies.[7−12]

MoS_2 has been used in ultra-low-friction studies. Formerly, the surface of three-dimensional graphitic MoS_2 was used for such experiments to achieve a friction coefficient of 10^{-3} along the sliding direction in its basal planes.[13] Recently, experiments[14,15] using friction force microscopy and theoretical calculations[16,17] on atomically thin sheets of MoS_2 confirmed the superlubricity of the hexagonal MoS_2 structure. In addition to superlubricity, other areas in which MoS_2 appears to be a potential material for various technological applications include hydrogen production,[18,19] hydrodesulfurization catalysis for removal of sulfur compounds from oil,[20−26] solar cells,[27] and photocatalysis.[28] Photoluminescence is measured in monolayer MoS_2, whereas it is absent in the graphitic structure.[29] Most recently, a transistor fabricated from single-layer MoS_2 exhibited superior features compared to graphene.[30] Studies to date suggest that MoS_2 might be promising for optoelectronic devices, solar cells, and light-emitting diodes.

Various properties revealed earlier for three-dimensional graphitic MoS_2 and presently for two-dimensional single-layer 1H-MoS_2 have made the functionalization of these structures by adatoms or vacancy defects a current issue. For example, ab initio calculations were carried for adsorption of thiophene[31] on catalytically active surface of crystalline MoS_2, which is used in hydrodesulfurization process. Similarly, the adsorption of aromatic (thiophene, benzothiophene, benzene, naphthalene, pyridine, quinoline) and conjugated (butadiene) compounds on the (0001) basal plane of MoS_2 has been studied.[32] Huang and Cho[33] investigated the adsorption of CO on the MoS_2 surface and calculated the relative energies of different reaction paths. In addition, the implementation of local magnetism through defects or impurities has been the focus of first-principles calculations. Fuhr et al.[34] found that neither S vacancy defects on the MoS_2 surface nor substitutional doping of Pd or Au induces a magnetic moment, whereas Fe and V induce magnetic moments when substituted for S atoms at the MoS_2 surface. Adsorption and substitutional doping of Nb atoms on the MoS_2 surface were also investigated.[35] Because magnetism based on sp orbitals yields longer-range exchange-coupling interactions than that based on d and f orbitals, inducing magnetic properties in MoS_2 monolayers through nonmagnetic adatoms has also been considered. Theoretical studies have concluded that H, B, C, N, and O atoms can significantly modify the magnetic and electronic properties of this material.[36]

In this article, we present a systematic study of the general effects of the adsorption of selected adatoms and vacancy defect on the electronic and magnetic properties of perfect 1H-MoS_2. Three issues are of particular interest: (i) How can the surface charge of a single layer of MoS_2 be enhanced through adatoms? (ii) How can spin polarization and a magnetic moment be induced in nonmagnetic 1H-MoS_2? (iii) How can the electronic and magnetic states be modified through adatoms and vacancy-induced localized gap states? We investigated 16 individual adatoms (i.e., C, Co, Cr, Fe, Ge, Mn, Mo, Ni, O, Pt, S, Sc, Si, Ti, V, and W) and 5 different types of vacancy defects (namely, Mo and S single vacancies, S_2 and MoS double vacancies, and

Received: January 3, 2011
Revised: May 24, 2011
Published: June 01, 2011

dx.doi.org/10.1021/jp2000442 | J. Phys. Chem. C 2011, 115, 13303–13311

MoS_2 triple vacancies) in view the above three issues and investigated their general features. Owing to the weak interlayer interaction present in MoS_2, predictions concerning functionalization of the 1H-MoS_2 honeycomb structure are expected to be relevant also for MoS_2 sheets comprising a few layers, as well as the surface of graphitic MoS_2.

METHODS

Our results are based on first-principles plane-wave calculations within density functional theory (DFT) using projector-augmented wave (PAW) potentials.[37] The exchange-correlation potential was approximated by the generalized gradient approximation (GGA) using the PW91[38] functional for both spin-polarized and spin-unpolarized cases. Although all discussions in the article are based on the results obtained within the GGA using PAW potentials, calculations within the local density approximation[39] (LDA) using PAW potentials were also performed for specific cases for the purpose of comparison. All structures were subjected to periodic boundary conditions using a supercell geometry. The kinetic energy cutoff and Brillouin zone (BZ) sampling were determined after extensive convergence analysis. A large spacing of ~10 Å between two-dimensional single layers of MoS_2 was used to hinder interlayer coupling. A plane-wave basis set with a kinetic energy cutoff of 600 eV was used. In the self-consistent field potential and total energy calculations, the BZ was sampled by special k points.[40] The numbers of these k points were $(35 \times 35 \times 1)$ for the unit cell and $(5 \times 5 \times 1)$ for adatom adsorption in a (4×4) supercell of 1H-MoS_2. All atomic positions and lattice constants were optimized using the conjugate gradient method, where the total energy and atomic forces were minimized. The convergence criterion for energy was chosen to be 10^{-5} eV between two consecutive steps, and the maximum Hellmann−Feynman force acting on each atom was less than 0.02 eV/Å upon ionic relaxation. The pressure in the unit cell was kept below 1 kBar. Numerical calculations were performed using the Vienna ab initio simulation package (VASP).[41,42]

Because DFT within the GGA underestimates the band gap, frequency-dependent GW_0 calculations[43] were carried out to correct the band gaps. The screened Coulomb potential, W, was kept fixed to the initial DFT value W_0, and the Green's function, G, was iterated four times. Various tests regarding vacuum separation, kinetic energy cutoff value, number of bands, k points, and grid points were performed. The final results for the GW_0 corrections were obtained using $(12 \times 12 \times 1)$ k points in the BZ, a 400 eV cutoff potential, 192 bands, and 64 grid points for 1H-MoS_2. We were not able to apply GW_0 corrections for adatoms and vacancies because of the large numbers of atoms in the supercells.

TWO-DIMENSIONAL HONEYCOMB STRUCTURE OF MOS_2

To reveal the effects of adatoms and vacancy defects, we first present our results related to the atomic, electronic, and magnetic properties of 1H-MoS_2, which were obtained using the same calculation parameters. In Figure 1a, we schematically illustrate the hexagonal crystal lattice, resulting in a honeycomb structure. The contour plots of total charge density, $\rho(\mathbf{r}) = \Sigma^{occ}|\Psi(k,\mathbf{r})|^2$, and isosurfaces of the charge-density difference, $\Delta\rho(\mathbf{r})$ (which was obtained by subtracting the free-atom charge densities of Mo and S atoms from the total charge density of 1H-MoS_2), are also

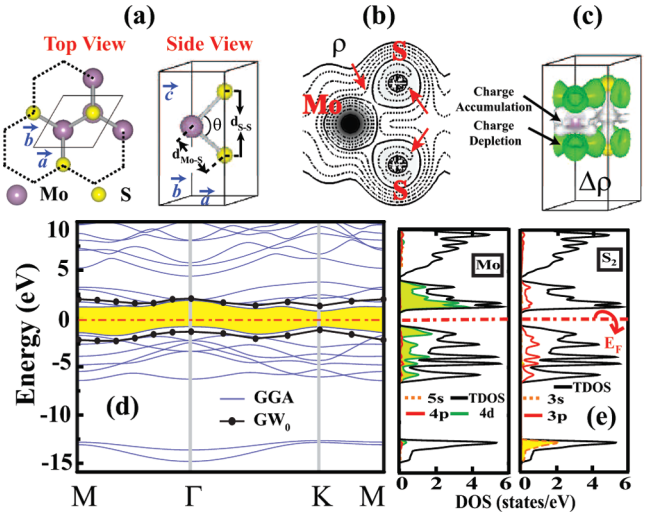

Figure 1. (a) Top and side views of the atomic structure of two-dimensional 1H-MoS_2 with a hexagonal lattice. The hexagonal unit cell with lattice constants $|a| = |b|$ is delineated by thin solid lines. The honeycomb structure consisting of Mo and S_2 atoms located at the corners is highlighted by dotted hexagons. (b) Contour plots of the charge density, ρ (see text for definition), in a vertical plane passing through Mo−S bonds. Arrows indicate the directions of increasing charge density. (c) Isosurface plot of the charge density difference, $\Delta\rho$ (see text for definition). The isosurface value was taken as 0.006 e/Å^3. (d) Energy band structure of 1H-MoS_2 calculated by GGA + PAW using the optimized structure. The zero of energy was set to the Fermi level indicated by the dash-dotted line. The gap between the valence and conduction bands is shaded; GW_0-corrected valence and conduction bands are shown by solid circles. (e) Total density of states (TDOS) and orbital-projected density of states (PDOS) for Mo and S.

shown in parts b and c, respectively, of Figure 1. There are ambiguities in determining the charge transfer, as calculated excess charges can depend on the method used. Although different methods result in different values for charge transfer (or excess charge on atoms), its direction can be predicted unambiguously. Based on Mulliken analysis,[46,47] the excess charge on each S atom and the depletion of electrons on each Mo atom were calculated to be 0.205 and 0.410 e, respectively. Bader analysis[48] yielded depletion of 1.2 electrons from Mo atoms and 0.6 excess electrons on each S atom. Electronic charge transferred from Mo to S atoms gives rise to an excess charge around S atoms. Consequently, 1H-MoS_2 can be viewed as a positively charged Mo plane sandwiched between two negatively charged planes of S atoms, as presented in Figure 1c. The repulsive Coulomb force between negatively charged S atoms facing each other in adjacent MoS_2 layers weakens the interlayer interaction in two individual 1H-MoS_2 layers (or a bilayer of MoS_2), as well as in graphitic MoS_2. In fact, the interaction between two adjacent MoS_2 layers in graphitic MoS_2 is repulsive even for large separations except for a slight attractive range (of only 7 meV without van der Waals interactions, but ~170 meV including van der Waals interactions) around the equilibrium separation. This is the main reason why MoS_2 flakes can be used to lower the friction coefficient in sliding friction. The cohesive energy of the optimized 1H-MoS_2 structure was found to be 15.55 eV per cell. For the known results, LDA + PAW calculations yielded stronger binding and, hence, a greater cohesive energy (E_C = 19.05 eV).

Table 1. Calculated Values of Single-Layer 1H-MoS_2 Lattice Constants ($|a| = |b|$), Bond Lengths (d_{Mo-S}, d_{S-S}), S−Mo−S Bond Angle [Θ(S−Mo−S)], Cohesive Energy per MoS_2 Unit (E_C), Direct Energy Band Gap (E_g), GW_0-Corrected Band Gap (E_{g+GW_0}), and Photoelectric Threshold (Φ)

method	a (Å)	d_{Mo-S} (Å)	d_{S-S} (Å)	θ(S−Mo−S) (deg)	E_C (eV)	E_g (eV)	E_{g+GW_0} (eV)	Φ (eV)
GGA + PAW	3.20	2.42	3.13	80.69	15.55	1.58	2.50	5.96
LDA + PAW	3.11	2.37	3.11	81.62	19.05	1.87	2.57	–
experiment	3.27,[44] 3.20[45]		–	–	–	–	–	–
theory	3.13[7]	2.41[7]	–	82.31[7]	15.6,[7] 14.99[9]	1.69,[7] 1.8,[9] 1.78,[8] 1.64[10]	–	–

The electronic structure of a two-dimensional suspended single layer of 1H-MoS_2 and the corresponding TDOS and PDOS calculated by the GGA + PAW approach are presented in Figure 1d,e. The states at the band edges, as well as at the lower-lying conduction band and the higher-lying valence band, originate from the hybridization of Mo 4d and S 3p orbitals. The direct band gap is E_g = 1.58 eV. The band gap calculated within by the LDA + PAW method is E_g = 1.87 eV, which is in good agreement with the band gap measured using complementary techniques of optical absorption, photoluminescence, and photoconductivity (1.90 eV).[5] Earlier, Bollinger et al.[10] predicted the band gap to be 1.64 eV using the GGA + ultrasoft pseudopotential approach. However, with a similar computational method, Li and Galli[12] calculated the band gap to be 1.80 eV. Li et al.[7] calculated the direct band gap as 1.69 eV by the GGA + PAW approach using a relatively smaller energy cutoff. Mendez et al.[9] found the direct band gap within the LDA to be E_g = 1.8 eV using a local basis set.[49] Lebegue and Eriksson[8] carried out LDA + PAW calculations using experimental lattice constants and found the band gap to be 1.78 eV. The band gap calculated in the present work is in fair agreement with previous studies.[7,9,10] However, we show that band gaps determined in earlier studies increase ∼1 eV upon GW_0 correction. The band gap calculated by the GGA (LDA) + PAW approach was corrected using the self-energy method GW_0 to be 2.50 (2.57) eV. The corrected band gap is ∼0.6−0.7 eV larger than the value measured experimentally.[5] The situation with graphitic MoS_2, which consists of stacked 1H-MoS_2 layers, however, is different. The indirect band gap of graphitic MoS_2 calculated by the GGA (LDA) + PAW method is 0.85 (0.72) eV and is corrected to be 1.44 (1.28) eV. In particular, the LDA + PAW band gap corrected by GW_0 is in good agreement with the experimental value.[50] Because LDA/GGA is designed to describe systems with slowly varying electron densities and can fail to model localized d orbitals,[51] more accurate band gap calculations can be carried out using the screened nonlocal exchange Heyd−Scuseria−Ernzerhof (HSE) functional of the generalized Kohn−Sham scheme.[52] Starting from the nonlocal charge density and wave functions, we calculated HSE- and G_0W_0 (both the screened Coulomb potential, W, and the Green's function, G, are kept fixed to the initial DFT value, W_0 and G_0 respectively)[51]-corrected electronic band structure of MoS_2 as a direct band gap of 2.23 and 2.78 eV, respectively. Surprisingly, the band gap of two-dimensional 1H-MoS_2 is overestimated by GW_0 correction. Here, we note that the band gap of two-dimensional fluorographene CF is also overestimated upon GW_0 correction.[53] In Table 1, we list all of the calculated structural parameters (including both lattice constants and internal parameters), cohesive energy, direct and GW_0-corrected band gaps, and photoelectric threshold of two-dimensional 1H-MoS_2.

Finally, we emphasize two important dimensionality effects related to the electronic structure of MoS_2 that have important consequences such as photoluminescence: (i) Upon going from graphitic MoS_2 to single-layer 1H-MoS_2, the energy band gap changes from indirect to direct. (ii) The minimum gap increases by ∼0.6 eV. The transformation from indirect to direct gap is related to the orbital composition of states at the edges of the conduction and valence bands.[12,29] The widening of the band gap in two-dimensional MoS_2 occurs because of the absence of the S p_z orbital interaction between adjacent MoS_2 layers and appears as the manifestation of the quantum confinement in the direction perpendicular to the MoS_2 layer.[5]

FUNCTIONALIZATION BY ADATOM ADSORPTION

The adsorption of adatoms is a widely used and efficient way to provide new functionalities to structures in nanoscale applications.[54−60] Among 16 different adatoms, namely, C, Co, Cr, Fe, Ge, Mn, Mo, Ni, O, Pt, S, Sc, Si, Ti, V, and W, we were interested in 10 transition-metal elements to determine ones that can induce magnetization in nonmagnetic 1H-MoS_2. Group 4A elements, namely, C, Si, and Ge, were considered because these atoms can form stable, planar, or buckled honeycomb structures.[61−63] Carbon was of particular interest for the fabrication of graphene + MoS_2 complexes or nanomeshes. Being the host atoms in 1H-MoS_2, Mo and S can exist as residues. Whether MoS_2 can be oxidized is an important issue that might limit future applications. The first question one has to address is, of course, whether these adatoms can form strong and stable bonds with 1H-MoS_2. The equilibrium adsorption sites of these 16 atoms were determined by first placing them at one of four different adsorption sites and subsequently optimizing the whole structure. Four possible adsorption sites considered initially for each adatom before the structure optimization include (i) the hollow site slightly above the center of the hexagon on the Mo atomic plane, (ii) the hollow site above the center of the hexagon on the S plane, (iii) the site on top of a Mo atom, and (iv) the site on top of a S atom. Here, the bridge site above a Mo−S bond is very similar to the site on top of a Mo atom. To avoid adatom−adatom coupling, a (4 × 4) supercell of 1H-MoS_2 was used, where the nearest adatom−adatom distance was ∼12.8 Å. Thus, the results can be related to the adsorption of an isolated adatom. The minimum-energy positions of adatoms after the optimization process are depicted in Figure 2. We note that C, Co, Fe, O, Ti, V, and W have two different binding sites (one having higher binding energy, E_b) that lead to dramatically different electronic and magnetic structures. Six distinct adsorption sites depicted in Figure 2, namely, Mo-1, Mo-2, S-1, S-2, S-3, and S-4, were distinguished after structure optimization.

All relevant data obtained from our calculations of adatoms adsorbed onto 1H-MoS_2 are presented in Table 2. The height of the adatom from the Mo and S planes were calculated relative to the average heights of Mo and S atoms in the

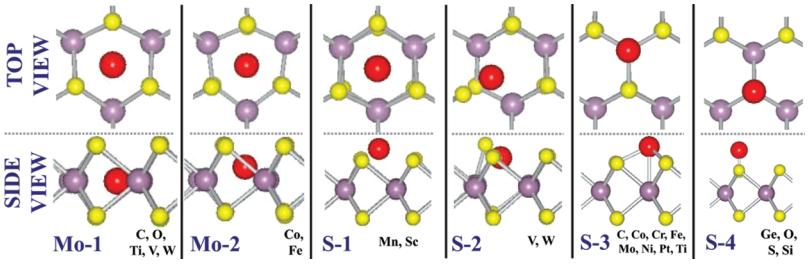

Figure 2. Top- and side-view schematic representations of possible adsorption geometries of adatoms obtained after structure optimization. Adatoms and host Mo and S atoms are represented by red, purple, and yellow balls, respectively. Side views clarify the heights of adatoms from the Mo and S atomic planes. Different adsorption sites are specified below each entry as Mo-*x* or S-*x*, where Mo (S) indicates that the adatoms were placed initially (before structure optimization) on the Mo (S) plane. In the Mo-1 and Mo-2 geometries, the adatoms are in and slightly above the Mo layer, respectively. The S-1−S-4 positions are associated with the S layer. The adatoms adsorbed at each site are given at the lower right-hand side of each entry.

Table 2. Calculated Values for the Properties of 16 Adatoms Adsorbed on 1H-MoS_2

atom	site[a]	h_{Mo}[b] (Å)	h_S[c] (Å)	d_{Mo}[d] (Å)	d_S[e] (Å)	E_b[f] (eV)	μ_T[g] (μ_B)	ρ^*[h] (e)	Φ[i] (eV)	P[j] (e Å)	E_i[k] (eV)
C	Mo-1	−0.01	1.56	2.04	2.44	3.28	NM[l]	−0.65	5.81	0.00	**0.14**, **0.19**, 2.18, 4.85
	S-3	1.58	−0.05	2.07	1.80	2.69	2.00	−0.58	5.74	−0.10	**0.26** ↑, **0.30** ↓, **1.07** ↑, **1.13** ↑, 1.55 ↓, 1.60 ↓
Co	Mo-2	0.61	0.99	2.22	2.19	0.96	1.00	0.15	5.57	−0.07	**0.61** ↑, **0.66** ↑, **0.82** ↓, **0.87** ↓, **0.89** ↑, 1.13 ↓
	S-3	2.52	0.94	2.56	2.11	2.92	1.00	0.44	5.17	−0.38	**0.29** ↑, **0.51** ↑, **0.57** ↓, **0.62** ↑, **0.99** ↓, 1.00 ↓
Cr	S-3	2.79	1.21	2.77	2.26	1.08	4.00	0.91	4.25	−0.75	**0.19** ↑, **0.22** ↑, **0.59** ↑, **0.64** ↑, **0.68** ↑, **1.60** ↓, 1.73 ↓
Fe	Mo-2	0.31	1.29	2.21	2.26	0.39	2.00	0.34	5.07	−0.04	**0.32** ↑, **0.48** ↑, **0.87** ↑, **1.01** ↓, 1.15 ↓, 1.32 ↓
	S-3	2.52	0.93	2.53	2.14	2.42	2.00	0.59	4.99	−0.46	**−0.03** ↑, **0.18** ↑, **0.21** ↑, **0.22** ↑, **0.91** ↓, **0.93** ↓, 1.31 ↓
Ge	S-4	3.83	2.26	4.28	2.30	1.18	2.00	0.39	4.78	−0.27	**1.10** ↑, **1.11** ↑, 1.72 ↓, 1.75 ↓
Mn	S-1	2.51	0.93	3.06	2.15	1.37	3.00	0.81	4.75	−0.44	**0.16** ↑, **0.17** ↑, **0.49** ↑, **0.50** ↑, **1.30** ↓, 1.98 ↓, 2.05 ↓
Mo	S-3	2.89	1.31	2.84	2.30	1.43	4.00	0.81	4.54	−0.76	**0.48** ↑, **0.79** ↑, **0.87** ↑, **0.91** ↑, 1.16 ↓, 1.42 ↓, 1.54 ↓
Ni	S-3	2.52	0.94	2.56	2.12	3.65	NM	0.36	5.58	−0.31	**0.12**, **0.16**, **0.21**, **0.50**, **0.51**, **0.57**
O	Mo-1	−0.01	1.57	1.95	2.56	2.24	NM	−1.11	5.72	0.00	**−6.36**, **−6.34**, **−5.66**, **0.32**
	S-4	2.94	1.38	3.51	1.49	3.99	NM	−0.91	5.96	0.35	**−5.63**, **−1.16**, **−0.90**
Pt	S-3	2.78	1.21	2.76	2.31	2.92	NM	0.08	5.66	−0.26	**0.26**, **0.27**, **0.37**, 1.76
S	S-4	3.48	1.91	3.96	1.94	2.17	NM	−0.11	5.96	0.23	**0.00**, **0.06**, **0.11**
Sc	S-1	2.84	1.25	3.30	2.29	2.63	1.00	1.45	4.31	−1.18	**1.28** ↑, **1.31** ↑, **1.35** ↓, 1.49 ↓, 2.25 ↓, 2.39 ↑
Si	S-4	3.73	2.16	4.18	2.17	1.39	2.00	0.58	4.94	−0.14	**0.98** ↑, **0.99** ↑, 1.65 ↓, 1.68 ↓
Ti	Mo-1	0.00	1.58	2.31	2.42	1.23	NM	1.14	5.71	0.00	**0.26**, **0.34**, **0.36**, 1.74, 1.77
	S-3	2.95	1.38	2.99	2.32	2.62	4.00	1.16	4.32	−1.12	**1.18** ↑, **1.24** ↑, **1.35** ↑, **1.37** ↑, 1.54 ↑, 1.77 ↓, 1.81 ↓
V	Mo-1	0.03	1.55	2.95	2.34	1.25	1.00	1.05	4.61	0.00	**0.12** ↑, **0.16** ↓, **0.17** ↑, **0.21** ↓, **1.54** ↑, 1.67 ↑, 1.69 ↓
	S-2	1.87	0.19	2.56	2.07	2.76	1.00	1.05	5.18	0.04	**0.07** ↑, **0.18** ↓, **0.84** ↑, 1.23 ↓, 1.45 ↑, 1.54 ↓
W	Mo-1	0.01	1.58	2.41	2.42	1.18	2.00	1.05	4.66	0.01	**0.16** ↑, **0.21** ↓, **1.41** ↑, **1.49** ↑, 1.61 ↓, 1.81 ↓
	S-2	1.87	0.16	2.61	2.15	4.93	NM	0.85	5.58	0.12	**0.13**, **0.19**, **0.58**, 1.57, 1.75

[a] For specific adatoms, the first and second lines are associated with adsorption to the Mo-layer and S-layer sites, respectively. Other adatoms have only positive binding energies when adsorbed to the S-layer site. Adsorption sites of adatoms are described in Figure 2 [b] Height of the adatom from the Mo layer. [c] Height of the adatom from the nearest S layer. [d] Distance from the adatom to the nearest Mo atom. [e] Distance from the adatom to the nearest S atom. [f] Adatom binding energy. [g] Magnetic moment per supercell. [h] Excess charge on the adatom (where a negative sign indicates excess electrons). [i] Photoelectric threshold (work function). [j] Dipole moment calculated in the direction normal to 1H-MoS_2 surface. [k] Energies of localized states induced by adatoms, as measured from the top of the valence band. Occupied states are indicated in bold, and their spin alignments are denoted as either spin-up (↑) or spin-down (↓). States without the arrow sign indicating spin alignment are nonmagnetic. [l] NM indicates a nonmagnetic state with net $\mu = 0\ \mu_B$.

corresponding planes. The binding energy, E_b, was calculated as $E_b = E_{ad} + E_{MoS_2} - E_{ad+MoS_2}$. Here, E_{ad} is the ground-state energy of the free adatom calculated in the same supercell with the same parameters, E_{MoS_2} is the total energy of the (4 × 4) supercell of 1H-MoS_2, and $E_{ad+MoS2}$ is the optimized total energy of the system adatom + (4 × 4) supercell of 1H-MoS_2. Among different adatoms studied here, Cr has the weakest binding energy (E_b =1.08 eV), whereas W has the strongest binding (E_b = 4.93 eV) and creates a local reconstruction on the S layer. The excess charge[48] of the adatom, ρ^*, was obtained by subtracting the calculated charge at the adatom, ρ_A, from the valence charge of the adatom, Z_A, that is, $\rho^* = Z_A - \rho_A$. Accordingly, $\rho^* < 0$ implies excess electron charge at the adatom site. The magnetic moments were obtained by carrying out spin-polarized calculations without assigning initial atomic magnetic moments to the adatoms. Upon relaxation, the final magnetic moment was obtained.

Because the adatom−adatom interaction is hindered by a large separation between adatoms, the adatoms presented in Table 2 give rise to localized electronic states in the band gap and resonant states in the band continua and, hence, modify the

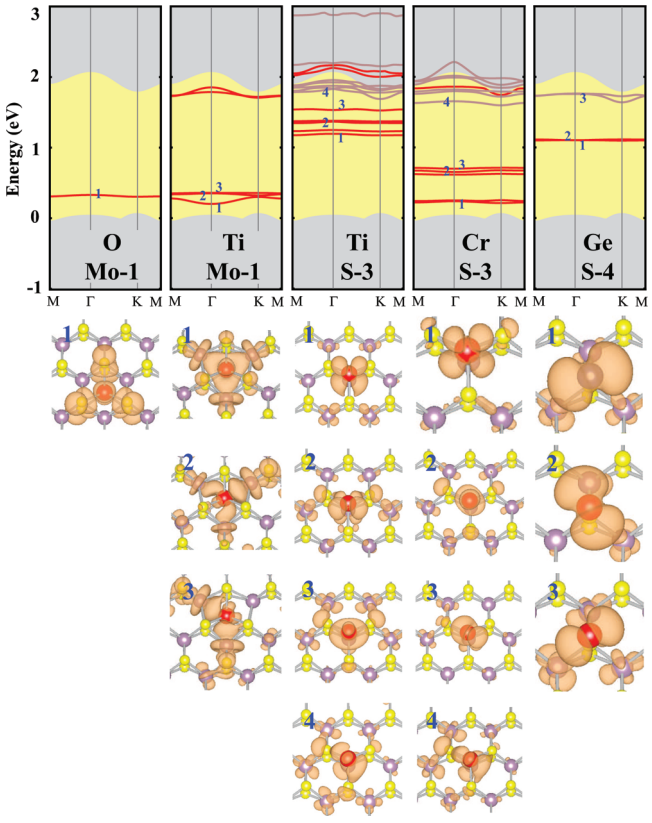

Figure 3. Schematic diagram of the relevant energy levels (or bands) of single adatoms (O, Ti, Cr, and Ge) adsorbed to each (4 × 4) supercell of 1H-MoS_2. The gray region in the background represents the valence- and conduction-band continua. For the nonmagnetic case, red bands contain more than 50% adatoms orbitals. For magnetic case, spin-up and spin-down bands are indicated by red and brown lines, respectively. Solid bands indicate that the contribution of the adatom to the band is more than 50%. In the lower part of each panel, the adsorption site is indicated according to the labeling scheme of Figure 2. Charge-density isosurfaces of adatom states specified by numerals are shown below. The isosurface value was taken as 2×10^{-5} e/Å^3.

electronic properties of 1H-MoS_2. In Figure 3, localized states of O, Ti, Cr, and Ge together with band-decomposed charge-density isosurfaces are presented. These atoms were specifically selected because they are representatives of some of the adatoms presented in Table 2. An oxygen adatom, when placed on the S plane, is adsorbed on top of a S atom (site S-4) with a binding energy of 3.99 eV. This site is in agreement with the results of He et al.[36] However, we also predicted a local minimum at site Mo-1 with a relatively smaller binding energy (E_b = 2.44 eV). Adsorbed O is nonmagnetic at both sites. Oxygen adatoms having the highest electronegativity and highest negative excess charge among all other adatoms have localized states in the valence band. When O is adsorbed at site Mo-l, the only localized state occurring in the band gap is filled and originates from a combination of the O p_z orbital with the p orbitals of the nearest S atoms. Being in the same group as O, sulfur displays similar electronic properties and has localized states in the band gap just above the valence band originating from its p_x and p_y orbitals.

Titanium can be adsorbed onto both Mo and S layers. In Figure 3, localized states of both adsorption geometries are indicated. When Ti is adsorbed on site Mo-l, the nearest d_{z^2} orbitals of the Mo atoms play an important role in the binding mechanism. The charge-density isosurface of the state numbered 1 in Figure 3 is dominated by the Ti d_{z^2} orbital, whereas isosurfaces 2 and 3 are dominated by the d_{xy} and $d_{x^2-y^2}$ orbitals, respectively, of Ti, which are parallel to the Mo layer. As for Ti adsorbed at site S-3, the Ti d_{xy} and d_{xz} orbitals dominate the states numbered 1 and 2, but the state numbered 3 originates mainly from the Ti d_{z^2} orbital. Cr and Mo adatoms at site S-3 on the 1H-MoS_2 surface have four singly occupied d states, but the d_{xy} state is doubly occupied. The Cr s and Mo s orbitals are vacant in both adatoms. Hence, Cr and Mo have local magnetic moments of $\mu = 4\ \mu_B$. For a W adatom at site S-2, the localized magnetic moment of $\mu = 2\ \mu_B$ occurs from the spin-polarized d orbitals of W together with the p orbitals of the nearest S atom.

The carbon adatom is of particular interest. Previously, He et al.[36] found that the lowest-energy adsorption position of a C adatom occurs in the plane of sulfur atoms on top of a Mo atom (i.e., at site S-3 shown in Figure 2). Here, we found the same site with a binding energy of E_b = 2.69 eV. However, a C adatom can go over a shallow barrier to a more stable adsorption position, namely, site Mo-1 with E_b = 3.28 eV at the center of three Mo atoms below the plane of S atoms. In Figure 4, we present a detailed analysis of these two adsorption sites. For site Mo-1, sp^2-hybridized orbitals of the C adatom and d_{xy} and $d_{x^2-y^2}$ orbitals of the three surrounding Mo atoms form three bonds, but the system remains nonmagnetic. In the case of site S-3, sp^2-hybridized orbitals of the C adatom form three bonds with the orbitals of the three surrounding S atoms of 1H-MoS_2. The interaction of the p_z orbital of the C adatom with the underlying Mo d_{z^2} orbitals results in a significant charge transfer from Mo to the C adatom. This creates a local magnetic moment of $\mu = 2\ \mu_B$ on the Mo atom. The charge-density contour plots in parts b and c of Figure 4 in the perpendicular and lateral planes, respectively, show the bonding configuration. Recently, a peculiar growth process in which carbon adatoms adsorbed on graphene readily diffuse above room temperature and nucleate segments of linear carbon chains (CACs) attached to graphene is predicted.[64] The calculated diffusion barrier on graphene was reported to be 0.37 eV. The energy difference of the C adatom between different adsorption sites, namely, S-3 and S-4, is 0.45 eV and comparable to that of a C atom on graphene. Here, we went beyond the adsorption of individual atoms and addressed the question of whether carbon adatoms can also lead to the formation of CACs on 1H-MoS_2. Unlike for single C adatom adsorption on 1H-MoS_2, CACs (starting from C_2) prefer to adsorb on top of S atoms as shown in Figure 4d,e. When attached to 1H-MoS_2, CACs favor cumulene-like structures with slightly alternating bonds and with a different kind of even−odd disparity. Therefore, the top-site geometry occurs because of the double sp + π-bonding within cumulene. Similar to the case in graphene, the binding energy of CACs having even numbers of C atoms are greater than those having odd number of C atoms. Even though CACs on graphene are nonmagnetic structures, odd-number CACs on 1H-MoS_2 have a magnetic moment of 2 μ_B arising from C atoms at the edges of the CAC.

Because the atomic radii of the other group 4A elements, namely, Si and Ge, are larger than that of C adatoms, the adsorption geometry differs from the adsorption site of C at site S-3. Si and Ge can be adsorbed only on the S plane at site S-4 and attain a local magnetic moment of $\mu = 2\ \mu_B$. This is a crucial result, because magnetic properties of MoS_2 monolayers are implemented through nonmagnetic adatoms.

The excess charge on the adatom (which is denoted as ρ^* in Table 2) and the position of the highest localized state in the gap

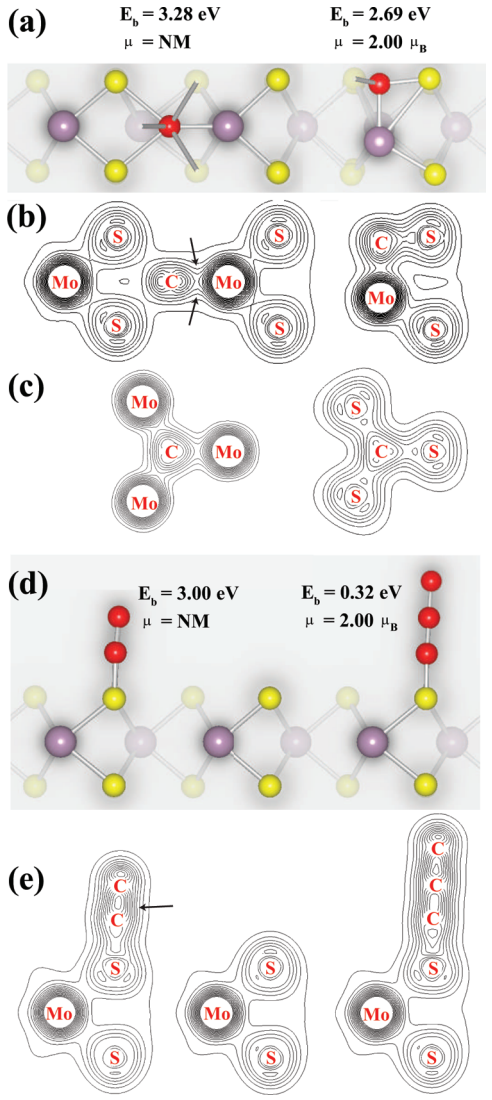

Figure 4. Analysis of bonding configurations of C adatoms on 1H-MoS_2. (a) Geometries of a single C adatom adsorbed in the Mo plane (left) and in the S plane (right). Adatoms and host Mo and S atoms are represented by red, purple, and yellow balls, respectively. (b) Contour plots of the total charge density on the plane passing through the atoms and bonds highlighted (not shaded) in panel a. (c) Contour plots of the total charge density on the horizontal plane passing through the Mo−C and S−C bonds parallel to 1H-MoS_2. (d) Adsorption geometries and energetics of C_2 and C_3 on 1H-MoS_2. (e) Contour plots of the total charge density on the vertical plane passing through the atoms and bonds highlighted (not shaded) in panel d. The arrows indicate the directions of increasing charge density.

are correlated with the adatom's electronegativity. For example, among C, Si, and Ge, C has the highest electronegativity. Whereas C has a negative excess charge, Si and Ge becomes positively charged when adsorbed. The calculated dipole moment for the system of a C adatom adsorbed on a S layer is diminished because of local reconstruction. Whereas adsorbed C, O, and S adatoms have excess electrons, all other adatoms in Table 2 are positively charged. Vanadium and W adsorbed at site S-2 have significant positive charges, but both induce minute electric dipole moment because of local reconstruction. Finally, it should be noted that excess charging of surfaces of 1H-MoS_2 by a higher level of coverage of specific adatoms can improve their functionalities in tribology.

Table 3. Calculated Vacancy Energies (E_V), Magnetic Moments (μ), and Energies of Localized States[a] in the Band Gap Measured from the Top of the Valence Band (E_i, eV) for Five Different Types of Vacancy Defects, Namely, Mo, MoS, MoS^2, S, and S_2, in the (7 × 7) Supercell of 1H-MoS_2

vacancy defect type:	Mo	MoS	MoS_2	S	S_2
E_V (eV):	13.44	17.36	22.63	5.89	11.74
μ (μ_B):	NM[b]	NM	2.00	5.89	NM
E_1	**0.26**	**0.15**	**0.15** ↑	**0.12**	**0.12**
E_2	**0.27**	**0.25**	**0.16** ↑	1.22	1.17
E_3	0.61	0.54	**0.25** ↓	1.23	1.19
E_4	1.02	0.69	**0.28** ↑		
E_5		1.21	0.53 ↓		
E_6		1.36	0.73 ↑		

[a] Localized states that are occupied are indicated in bold, and their spin alignments are denoted as either spin-up (↑) or spin-down (↓). States without an indication of spin alignment are nonmagnetic. [b] NM indicates a nonmagnetic state with net $\mu = 0\ \mu_B$.

VACANCY DEFECTS

It is known that vacancy defects in two-dimensional graphene,[65−69] graphene nanoribbons,[70,71] two-dimensional graphane,[72] and graphane nanoribbons[73] give rise to crucial changes in the electronic and magnetic structure. According to Lieb's theorem,[74] the net magnetic moment of the structure occurs because of the difference in the number of atoms belonging to different sublattices A and B, that is, $\mu = (N_A - N_B)\mu_B$. Although magnetic moments calculated using DFT for vacancies in two-dimensional graphene and armchair graphene nanoribbons generally confirmed Lieb's theorem, the results were diversified for vacancies in zigzag graphene nanoribbons[70,71] because of coupling with magnetic edge states. In the case of 1H-MoS_2, Lieb's theorem cannot be directly applicable, even if alternating Mo and S units form a honeycomb structure. We investigated five different types of vacancy defects that are formed in two-dimensional 1H-MoS_2, namely, Mo and S single vacancies, MoS and S_2 double vacancies, and MoS_2 triple vacancies. All structures were optimized upon the creation of a particular type of vacancy. Vacancy energies, E_V, were calculated by subtracting the total energy of the perfect structure (without any vacancy) from the sum of the total energy of a structure having a particular type of vacancy and the total energy(ies) of missing atoms in the vacancy defect. Here all structures are optimized in their ground states (whether magnetic or nonmagnetic). A positive E_V value indicates that the formation of the vacancy defect is an endothermic process. In Table 3, vacancy energies as defined above and their magnetic ground states are presented. We note that the equilibrium concentrations of vacancies are usually very low because of their high formation energies. Nonetheless, new techniques have been developed to create defects, which also makes the generation of nanomesh vacancies possible.[75−77]

We carried out calculations on vacancy defects of Mo, S, and S_2, in the (2 × 2), (4 × 4), and (7 × 7) supercells of the 1H-MoS_2 structure. Even if relatively larger sizes of supercells are not affected, the size of supercell is contracted upon creating a

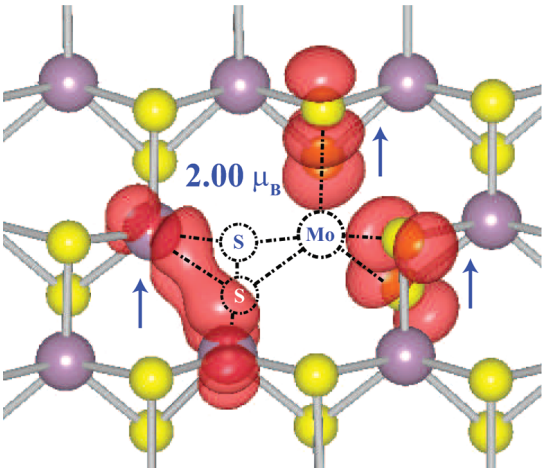

Figure 5. Isosurfaces of the charge-density difference of a MoS_2 vacancy defect in the (7×7) supercell of 1H-MoS_2. Dashed atoms and bonds are vacant sites. The charge-density difference was obtained from the difference between the spin-up and spin-down charge densities ($\Delta\rho_{\uparrow,\downarrow} = \rho_{\uparrow} - \rho_{\downarrow}$). The total magnetic moment was calculated as 2 μ_B. Up arrows indicate reions of excess spin-up charge. The isosurface value was taken as 3×10^{-3} eV/Å^3.

vacancy defect in the (2×2) supercell. In addition, we also considered MoS double vacancies and MoS_2 triple vacancies in (7×7) supercells. For all of these supercell sizes including the (7×7) supercell, we carried out calculations with many different initial magnetic moment configurations, but for all of the vacancy defects, except MoS_2 triple vacancy, the magnetic moment on any of the atoms in the supercell vanished. To justify these results, we also repeated the calculations using the LDA + PAW approach, which also results in a magnetic state for MoS_2 triple vacancy having a net magnetic moment of $\mu_T = 2\,\mu_B$. We seek the origin of magnetic states in the charge transfer between Mo and S and hence examined charge densities around the vacancy defects using Bader analysis.[48] In the case of S and S_2 vacancy defects, the excess (positive) charge on the nearest Mo adatoms around the vacancy slightly decreases, and hence does not cause any magnetic moment. The charge transfers and resulting excess charges around Mo and MoS_2 vacancies are affected even up to third-nearest-neighbor atoms. For example, S atoms around a Mo vacancy have 0.1 *e* less charge, because the third Mo atom, which provides excess electrons to S is missing. However, these S atoms surrounding the Mo vacancy receive more charge from the two Mo atoms. Similar cases were also investigated for MoS vacancy defects. Nonetheless, the charge transfers in the close proximity of S, S_2, Mo, and MoS vacancies are not significant as compared to those of the perfect structure, and consequently, they do not lead to a magnetic state. Interestingly, the disturbances in the charge transfer due to MoS_2 the triple vacancy are significant and result in the magnetic state at the close proximity of the defect.

In Figure 5, we present the isosurfaces of the difference in charge density between the spin-up and spin-down states (i.e., $\Delta\rho_{\uparrow,\downarrow} = \rho_{\uparrow} - \rho_{\downarrow}$) at the close proximity of MoS_2 vacancy. After reconstruction around the vacancy, two Mo and four S atoms have dangling bonds. In this case, the Mo atoms having dangling bonds are also less positively charged, and the S atoms having dangling bonds are less negatively charged compared to those in perfect MoS_2. However, in comparison with S, S_2, Mo, and MoS vacancies the amount of charge transfers here are almost doubled to cause to significant disturbances and spin polarization. The total magnetic moment of 2 μ_B are originated equally from d_{yz} and d_{zx} orbitals of Mo and p orbitals of S which have dangling bonds as seen in Figure 5. The nonmagnetic state is ~130 meV energetically less favorable. These results are also consistent with the vacancy defects in armchair-edged MoS_2 nanoribbons.[11] Electronically, vacancy defects give rise to states in the band gap that localized at atoms around the vacancy (see Table 3). Both the band gap and the electronic properties of 1H-MoS_2 are modified by these states.

DISCUSSION AND CONCLUSIONS

The adsorption of adatoms and creation of vacancy defects in two-dimensional single-layer MoS_2 honeycomb structure have crucial effects on the electronic and magnetic properties. We found that several adatoms can be adsorbed readily at diverse sites with significant binding energies. In this respect, MoS_2 appears to be a material that is suitable for functionalization. Whereas two-dimensional single-layer MoS_2 is a direct-band-gap semiconductor, magnetic or nonmagnetic localized gap states due to adatoms occur in the band gap and expand the capacity of this material in nanoelectronics and promise future applications. Additionally, two-dimensional sheets of MoS_2 can attain local magnetic moments through the adsorption of 3d transition-metal atoms, as well as Si and Ge. Because carbon is of particular interest, we also examined the adsorption of C_2 and linear C_3. Significant amounts of charge are transferred to (or from) adatoms. Excess surface charge at higher coverage of adatoms can improve the tribological and catalytic properties of 1H-MoS_2. Whereas vacancy defects of S, S_2, Mo, and MoS created in two-dimensional 1H-MoS_2 do not induce any magnetic moment, the creation of MoS_2 triple vacancies results in a significant magnetic moment in the system. Briefly, functionalization of the MoS_2 honeycomb structure through adatom adsorption and vacancy creation appears to be a promising way to extend the applications of MoS_2. Because the interlayer interaction in graphitic MoS_2 is a weak van der Waals interaction, the present results are also relevant for the surfaces of three-dimensional MoS_2.

AUTHOR INFORMATION

Corresponding Author

*E-mail: ciraci@fen.bilkent.edu.tr.

ACKNOWLEDGMENT

This work was supported by TUBITAK through Grants 104T537 and 108T234. Part of the computational resources were provided by UYBHM at Istanbul Technical University. S.C. acknowledges TUBA for partial support. We thank the DEISA Consortium (www.deisa.eu), funded through EU FP7 Project RI-222919, for support within the DEISA Extreme Computing Initiative.

REFERENCES

(1) Joensen, P.; Frindt, R.; Morrison, S. *Mater. Res. Bull.* **1986**, *21*, 457–461.

(2) Helveg, S.; Lauritsen, J.; Laegsgaard, E.; Stensgaard, I.; Norskov, J.; Clausen, B.; Topsoe, H.; Besenbacher, F. *Phys. Rev. Lett.* **2000**, *84*, 951–954.

(3) Lee, C.; Yan, H.; Brus, L. E.; Heinz, T. F.; Hone, J.; Ryu, S. *ACS Nano* **2010**, *4*, 2695–2700.
(4) Novoselov, K.; Jiang, D.; Schedin, F.; Booth, T.; Khotkevich, V.; Morozov, S.; Geim, A. *Proc. Natl. Acad. Sci. U.S.A.* **2005**, *102*, 10451–10453.
(5) Mak, K. F.; Lee, C.; Hone, J.; Shan, J.; Heinz, T. F. *Phys. Rev. Lett.* **2010**, *105*, 136805.
(6) Coleman, J. N.; Lotya, M.; O'Neill, A.; Bergin, S. D.; King, P. J.; Khan, U.; Young, K.; Gaucher, A.; De, S.; Smith, R. J.; Shvets, I. V.; Arora, S. K.; Stanton, G.; Kim, H.-Y.; Lee, K.; Kim, G. T.; Duesberg, G. S.; Hallam, T.; Boland, J. J.; Wang, J. J.; Donegan, J. F.; Grunlan, J. C.; Moriarty, G.; Shmeliov, A.; Nicholls, R. J.; Perkins, J. M.; Grieveson, E. M.; Theuwissen, K.; McComb, D. W.; Nellist, P. D.; Nicolosi, V. *Science* **2011**, *331*, 568–571.
(7) Li, Y.; Zhou, Z.; Zhang, S.; Chen, Z. *J. Am. Chem. Soc.* **2008**, *130*, 16739–16744.
(8) Lebegue, S.; Eriksson, O. *Phys. Rev. B* **2009**, *79*, 115409.
(9) Botello-Mendez, A. R.; Lopez-Urias, F.; Terrones, M.; Terrones, H. *Nanotechnology* **2009**, *20*, 325703.
(10) Bollinger, M.; Lauritsen, J.; Jacobsen, K.; Norskov, J.; Helveg, S.; Besenbacher, F. *Phys. Rev. Lett.* **2001**, *87*, 196803.
(11) Ataca, C.; Sahin, H.; Akturk, E.; Ciraci, S. *J. Phys. Chem. C* **2011**, *115*, 3934–3941.
(12) Li, T.; Galli, G. *J. Phys. Chem. C* **2007**, *111*, 16192–16196.
(13) Martin, J.; Donnet, C.; Lemogne, T.; Epicier, T. *Phys. Rev. B* **1993**, *48*, 10583–10586.
(14) Hoelscher, H.; Ebeling, D.; Schwarz, U. D. *Phys. Rev. Lett.* **2008**, *101*, 246105.
(15) Lee, C.; Li, Q.; Kalb, W.; Liu, X.-Z.; Berger, H.; Carpick, R. W.; Hone, J. *Science* **2010**, *328*, 76–80.
(16) Liang, T.; Sawyer, W. G.; Perry, S. S.; Sinnott, S. B.; Phillpot, S. R. *Phys. Rev. B* **2008**, *77*, 104105.
(17) Onodera, T.; Morita, Y.; Suzuki, A.; Koyama, M.; Tsuboi, H.; Hatakeyama, N.; Endou, A.; Takaba, H.; Kubo, M.; Dassenoy, F.; Minfray, C.; Joly-Pottuz, L.; Martin, J.-M.; Miyamoto, A. *J. Phys. Chem. B* **2009**, *113*, 16526–16536.
(18) Hinnemann, B.; Moses, P.; Bonde, J.; Jorgensen, K.; Nielsen, J.; Horch, S.; Chorkendorff, I.; Norskov, J. *J. Am. Chem. Soc.* **2005**, *127*, 5308–5309.
(19) Jaramillo, T. F.; Jorgensen, K. P.; Bonde, J.; Nielsen, J. H.; Horch, S.; Chorkendorff, I. *Science* **2007**, *317*, 100–102.
(20) Lauritsen, J.; Helveg, S.; Laegsgaard, E.; Stensgaard, I.; Clausen, B.; Topsoe, H.; Besenbacher, E. *J. Catal.* **2001**, *197*, 1–5.
(21) Lauritsen, J.; Bollinger, M.; Laegsgaard, E.; Jacobsen, K.; Norskov, J.; Clausen, B.; Topsoe, H.; Besenbacher, F. *J. Catal.* **2004**, *221*, 510–522.
(22) Lauritsen, J. V.; Kibsgaard, J.; Olesen, G. H.; Moses, P. G.; Hinnemann, B.; Helveg, S.; Norskov, J. K.; Clausen, B. S.; Topsoe, H.; Laegsgaard, E.; Besenbacher, F. *J. Catal.* **2007**, *249*, 220–233.
(23) Moses, P. G.; Hinnemann, B.; Topsoe, H.; Norskov, J. K. *J. Catal.* **2007**, *248*, 188–203.
(24) Raybaud, P.; Hafner, J.; Kresse, G.; Kasztelan, S.; Toulhoat, H. *J. Catal.* **2000**, *189*, 129–146.
(25) Sun, M.; Nelson, A.; Adjaye, J. *J. Catal.* **2004**, *226*, 32–40.
(26) Todorova, T.; Prins, R.; Weber, T. *J. Catal.* **2007**, *246*, 109–117.
(27) Kline, G.; Kam, K.; Ziegler, R.; Parkinson, B. *Sol. Energy Mater.* **1982**, *6*, 337–350.
(28) Wilcoxon, J.; Thurston, T.; Martin, J. *Nanostruct. Mater.* **1999**, *12*, 993–997.
(29) Splendiani, A.; Sun, L.; Zhang, Y.; Li, T.; Kim, J.; Chim, C.-Y.; Galli, G.; Wang, F. *Nano Lett.* **2010**, *10*, 1271–1275.
(30) Radisavljevic, B.; Radenovic, A.; Brivio, J.; Giacometti, V.; Kis, A. *Nat. Nanotechnol.* **2011**, *6*, 147–150.
(31) Raybaud, P.; Hafner, J.; Kresse, G.; Toulhoat, H. *Phys. Rev. Lett.* **1998**, *80*, 1481–1484.
(32) Moses, P. G.; Mortensen, J. J.; Lundqvist, B. I.; Norskov, J. K. *J. Chem. Phys.* **2009**, *130*, 104709.
(33) Huang, M.; Cho, K. *J. Phys. Chem. C* **2009**, *113*, 5238–5243.
(34) Fuhr, J.; Saul, A.; Sofo, J. *Phys. Rev. Lett.* **2004**, *92*, 026802.
(35) Ivanovskaya, V. V.; Zobelli, A.; Gloter, A.; Brun, N.; Serin, V.; Colliex, C. *Phys. Rev. B* **2008**, *78*, 134104.
(36) He, J.; Wu, K.; Sa, R.; Li, Q.; Wei, Y. *Appl. Phys. Lett.* **2010**, *96*, 082504.
(37) Blochl, P. *Phys. Rev. B* **1994**, *50*, 17953–17979.
(38) Perdew, J.; Chevary, J.; Vosko, S.; Jackson, K.; Pederson, M.; Singh, D.; Fiolhais, C. *Phys. Rev. B* **1992**, *46*, 6671–6687.
(39) Ceperley, D.; Alder, B. *Phys. Rev. Lett.* **1980**, *45*, 566–569.
(40) Monkhorst, H. J.; Pack, J. D. *Phys. Rev. B* **1976**, *13*, 5188–5192.
(41) Kresse, G.; Hafner, J. *Phys. Rev. B* **1993**, *47*, 558–561.
(42) Kresse, G.; Furthmuller, J. *Phys. Rev. B* **1996**, *54*, 11169–11186.
(43) Shishkin, M.; Kresse, G. *Phys. Rev. B* **2006**, *74*, 035101.
(44) Yang, D.; Sandoval, S.; Divigalpitiya, W.; Irwin, J.; Frindt, R. *Phys. Rev. B* **1991**, *43*, 12053–12056.
(45) Joensen, P.; Crozier, E.; Alberding, N.; Frindt, R. *J. Phys. C: Solid State Phys.* **1987**, *20*, 4043–4053.
(46) Mulliken, R. S. *J. Chem. Phys.* **1955**, *23*, 1841–1846.
(47) It should be kept in mind that there are ambiguities in calculating charge transfer. In fact, different methods result in different values of charge transfer.
(48) Henkelman, G.; Arnaldsson, A.; Jonsson, H. *Comput. Mater. Sci.* **2006**, *36*, 354–360.
(49) Soler, J.; Artacho, E.; Gale, J.; Garcia, A.; Junquera, J.; Ordejon, P.; Sanchez-Portal, D. *J. Phys.—Condens. Matter* **2002**, *14*, 2745–2779.
(50) Kam, K.; Parkinson, B. *J. Phys. Chem.* **1982**, *86*, 463–467.
(51) Fuchs, F.; Furthmüller, J.; Bechstedt, F.; Shishkin, M.; Kresse, G. *Phys. Rev. B* **2007**, *76*, 115109.
(52) Heyd, J.; Scuseria, G. E.; Ernzerhof, M. *J. Chem. Phys.* **2003**, *118*, 8207–8215.
(53) Şahin, H.; Topsakal, M.; Ciraci, S. *Phys. Rev. B* **2011**, *83*, 115432.
(54) Ataca, C.; Ciraci, S. *Phys. Rev. B* **2010**, *82*, 165402.
(55) Ataca, C.; Akturk, E.; Sahin, H.; Ciraci, S. *J. Appl. Phys.* **2011**, *109*, 013704.
(56) Akturk, E.; Ataca, C.; Ciraci, S. *Appl. Phys. Lett.* **2010**, *96*, 123112.
(57) Ataca, C.; Akturk, E.; Ciraci, S.; Ustunel, H. *Appl. Phys. Lett.* **2008**, *93*, 043123.
(58) Ataca, C.; Akturk, E.; Ciraci, S. *Phys. Rev. B* **2009**, *79*, 041406.
(59) Chan, K. T.; Neaton, J. B.; Cohen, M. L. *Phys. Rev. B* **2008**, *77*, 235430.
(60) Durgun, E.; Akman, N.; Ataca, C.; Ciraci, S. *Phys. Rev. B* **2007**, *76*, 245323.
(61) Novoselov, K.; Geim, A.; Morozov, S.; Jiang, D.; Zhang, Y.; Dubonos, S.; Grigorieva, I.; Firsov, A. *Science* **2004**, *306*, 666–669.
(62) Sahin, H.; Cahangirov, S.; Topsakal, M.; Bekaroglu, E.; Akturk, E.; Senger, R. T.; Ciraci, S. *Phys. Rev. B* **2009**, *80*, 155453.
(63) Cahangirov, S.; Topsakal, M.; Akturk, E.; Sahin, H.; Ciraci, S. *Phys. Rev. Lett.* **2009**, *102*, 236804.
(64) Ataca, C.; Ciraci, S. *Phys. Rev. B* **2011**, *83*, 235417.
(65) Esquinazi, P.; Spemann, D.; Hohne, R.; Setzer, A.; Han, K.; Butz, T. *Phys. Rev. Lett.* **2003**, *91*, 227201.
(66) Hashimoto, A.; Suenaga, K.; Gloter, A.; Urita, K.; Iijima, S. *Nature* **2004**, *430*, 870–873.
(67) Yazyev, O. V.; Helm, L. *Phys. Rev. B* **2007**, *75*, 125408.
(68) Vozmediano, M.; Lopez-Sancho, M.; Stauber, T.; Guinea, F. *Phys. Rev. B* **2005**, *72*, 155121.
(69) Brey, L.; Fertig, H. A.; Das Sarma, S. *Phys. Rev. Lett.* **2007**, *99*, 116802.
(70) Palacios, J. J.; Fernandez-Rossier, J.; Brey, L. *Phys. Rev. B* **2008**, *77*, 195428.
(71) Topsakal, M.; Akturk, E.; Sevincli, H.; Ciraci, S. *Phys. Rev. B* **2008**, *78*, 235435.
(72) Sahin, H.; Ataca, C.; Ciraci, S. *Appl. Phys. Lett.* **2009**, *95*, 222510.
(73) Sahin, H.; Ataca, C.; Ciraci, S. *Phys. Rev. B* **2010**, *81*, 205417.

(74) Lieb, E. *Phys. Rev. Lett.* **1989**, *62*, 1201–1204.
(75) Bai, J.; Zhong, X.; Jiang, S.; Huang, Y.; Duan, X. *Nat. Nanotechnol.* **2010**, *5*, 190–194.
(76) Lahiri, J.; Lin, Y.; Bozkurt, P.; Oleynik, I. I.; Batzill, M. *Nat. Nanotechnol.* **2010**, *5*, 326–329.
(77) Balog, R.; Jørgensen, B.; Nilsson, L.; Andersen, M.; Rienks, E.; Bianchi, M.; Fanetti, M.; Lægsgaard, E.; Baraldi, A.; Lizzit, S.; Sljivancanin, Z.; Besenbacher, F.; Hammer, B.; Pedersen, T. G.; Hofmann, P.; Hornekær, L. *Nat. Mater.* **2010**, *9*, 315–319.